

# 1 Pressure and ion composition boundaries at Mars

Shaosui Xu,<sup>1,2</sup> Michael W. Liemohn,<sup>2</sup> Chuanfei Dong,<sup>2,3</sup> David L. Mitchell,<sup>1</sup>

Stephen W. Bougher,<sup>2</sup> and Yingjuan Ma<sup>4</sup>

Corresponding author: Shaosui Xu, Space Science Laboratory, University of California, Berkeley, California, USA. (shaosui.xu@ssl.berkeley.edu)

<sup>1</sup>Space Science Laboratory, University of California Berkeley, California, USA.

<sup>2</sup>Department of Climate and Space Sciences and Engineering, University of Michigan, Ann Arbor, Michigan, USA.

<sup>3</sup>Princeton Plasma Physics Laboratory, Princeton University, Princeton, New Jersey, USA

<sup>4</sup>Institute of Geophysics and Planetary Physics, UCLA, Los Angeles, California, USA,

Author Manuscript

This is the author manuscript accepted for publication and has undergone full peer review but has not been through the copyediting, typesetting, pagination and proofreading process, which may lead to differences between this version and the Version of Record. Please cite this article

as doi:10.1002/2016JA022644 June 28, 2016, 11:31pm

D R A F T

**Abstract.**

This study analyzes results from a multifluid MHD simulation to investigate the shape and structure of the pressure and composition boundaries at Mars, which can provide physical insight for the observational analysis. These boundaries are examined via the unity contours and gradients of the plasma  $\beta$ , as well as  $\beta^*$ , which includes the dynamic pressure in the numerator, and the ion mass and number density ratios. It is found that unity contours are well aligned with the gradient extrema, indicating that the unity contour is a topological boundary. In addition, these two transitions of pressure and composition are of a thickness of  $0.05-0.1 R_M$  near the subsolar region to  $r=1.5 R_M$  in the tail. The comparison of the pressure and composition boundaries indicates that the two are very similar and that not only the plasma sheet but the full volume of the lobes are dominated by planetary ions. It suggests that the tail escape for ions not only concentrates in the central plasma sheet but also the magnetic lobes. It is also worthy pointing out that the ion number density ratio unity contour is found to be systematically smaller than other unity boundaries, which calls for attention when the ion number density is used to identify such boundaries. Finally, the comparison between the boundaries of this study and two analytical fittings is carried out. We found a good agreement with the Vignes fitting, with little flaring in the tail, in contrast to a larger flaring angle from the Trotignon fitting.

## 1. Introduction

24 *Moore and Delcourt* [1995] came up with the concept of the geopause, which marks  
25 the boundary between solar and terrestrial dominance of near-Earth space. Multiple  
26 geopause boundaries exist, depending on the parameter used to define the boundary. The  
27 magnetopause is the arguably the most well known of these geopause boundaries, but  
28 *Moore and Delcourt* [1995] also discussed the existence of plasma pressure and density  
29 geopauses. At such interfaces, energy and particle interchange between the solar wind and  
30 the planetary ionospheric plasmas could occur, resulting in dynamics and perturbations  
31 that are essential for geostorm development. Such a concept can be applied to other  
32 planets, such as Mars, to provide insight into the physics of magnetic topology and ion  
33 escape, as one way for cold planetary ions to attain escape energy is through such a  
34 coupling with the solar wind plasma at this interface.

35 Mars is usually classified as an unmagnetized planet in terms of the interaction with  
36 solar wind due to the absence of a significant global intrinsic magnetic field. This in-  
37 teraction results in several distinct regions, such as the magnetosheath, the magnetic  
38 pileup region, and the tail region [e.g. *Nagy et al.*, 2004; *Bertucci et al.*, 2012]. The  
39 existence of localized crustal fields [e.g. *Acuna et al.*, 1999] complicates this interaction  
40 [e.g. *Brain et al.*, 2003, 2007; *Harnett and Winglee*, 2005; *Liemohn et al.*, 2006, 2007; *Ma*  
41 *et al.*, 2014; *Dong et al.*, 2015a; *Xu et al.*, 2014]. The transition between the magne-  
42 tosheath and the magnetic pileup region has several observational characteristics, which  
43 have been identified by different instruments on various spacecraft. One feature is a sharp  
44 increase in magnetic field strength coincident with a decrease in field fluctuations, which

45 was observed by Phobos-2 [e.g. *Riedler et al.*, 1989], the Mars Global Surveyor (MGS)  
46 spacecraft [e.g. *Vignes et al.*, 2000; *Crider et al.*, 2002; *Bertucci et al.*, 2005] and also  
47 the Mars Atmosphere and Volatile Evolution (MAVEN) spacecraft [e.g. *Jakosky et al.*,  
48 2015a, b; *Connerney et al.*, 2015; *Halekas et al.*, 2015; *Matsunaga et al.*, 2015]. These  
49 observations resulted in the names known as the magnetic pileup boundary (MPB) or the  
50 induced magnetosphere boundary (IMB). Another feature of this transition is a switch  
51 from solar wind ions to planetary heavy ions, which was observed by Phobos-2 [e.g. *Sauer*  
52 *et al.*, 1992; *Trotignon et al.*, 1996], Mars Express [e.g. *Dubinin et al.*, 2006, 2008; *Fränz*  
53 *et al.*, 2006] and MAVEN [e.g. *Ma et al.*, 2015; *Dong et al.*, 2015b; *Matsunaga et al.*,  
54 2015]. This resulted in the names including the protonopause and the ion composition  
55 boundary (ICB). These boundaries located at the inner side of the magnetosheath were  
56 also identified and studied by plenty of simulation efforts [e.g. *Sauer et al.*, 1994; *Ma et al.*,  
57 2002, 2004; *Böswetter et al.*, 2004; *Brecht*, 1990, 1997; *Harnett and Winglee*, 2005; *Mod-*  
58 *olo et al.*, 2006; *Kallio et al.*, 2006; *Simon et al.*, 2007; *Brain et al.*, 2010]. In particular,  
59 *Fang et al.* [2015] showed the irregularity of MPB and how it varies with the crustal field  
60 rotation.

61 The transition between the magnetosheath and magnetic pileup region at Mars gener-  
62 ally resembles Earth's geopause, because of the sharp transitions between the solar wind  
63 and planetary plasmas. In this study, we analyze the results from a BATS-R-US Mars  
64 Multifluid MHD model to quantitatively study these boundaries by looking at plasma-  
65 type (thermal and dynamic) and magnetic pressures. There are different ways to define  
66 such boundaries, such as locations where the dominant contribution to the total pressure  
67 changes or where the dominant ion species changes, or where sharp gradients in the pres-

68 sure terms or composition occur. Pressure and composition boundaries often appear sharp  
69 on time series figures of spacecraft observations, particularly on the day side. Similarly,  
70 boundaries identified in simulations are often displayed as lines and surfaces. However,  
71 the thicknesses of these transitions are typically not considered, especially downstream  
72 of the terminator. Transition thicknesses can be determined both observationally and  
73 from simulations, which is useful for assessing the transition from solar wind to planetary  
74 influence. In addition, due to limitation of instruments of many spacecraft, the relation  
75 of MPB and ICB was not well understood. This study will also present a systematic  
76 comparison between the two from a theoretical view.

## 2. BATS-R-US Mars Multifluid MHD Model Description

77 The University of Michigan 3-D Block-Adaptive Tree Solarwind Roe-type Upwind  
78 Scheme (BATS-R-US) multifluid MHD (MF-MHD) model was initially developed for the  
79 Earth environment [Powell et al., 1999; Glocer et al., 2009; Tóth et al., 2012] and then  
80 adapted to Mars [Najib et al., 2011; Dong et al., 2014]. The Mars MF-MHD model com-  
81 putes a full set of continuity, momentum, and energy equations for four ion species,  $H^+$ ,  
82  $O^+$ ,  $O_2^+$ , and  $CO_2^+$ . Due to a much weaker magnetic environment at Mars, and thus a  
83 much slower Alfvén speed, the inner boundary of the Mars MF-MHD model is set at 100  
84 km altitude. This altitude is below the ionospheric density peak, thus the model is able  
85 to simulate the entire plasma environment around the planet.

86 The model includes detailed ionospheric chemistry, photoionization, charge exchange,  
87 recombination, and electron impact ionization. The chemical reaction schemes are de-  
88 scribed in Ma et al. [2004] and Najib et al. [2011]. Electron impact ionization rates are  
89 given by Cravens et al. [1987] and collision frequencies between species are given by Schunk

90 *and Nagy* [2009]. At the inner boundary,  $O^+$ ,  $O_2^+$ , and  $CO_2^+$  are assumed to be in photochemical equilibrium and  $H^+$  is set to be approximately 30% of the solar wind density, 91 to account for proton penetration into the ionosphere. Additionally, the velocity  $u$  is set 92 to be a reflective boundary condition. Furthermore, the ion and electron temperature 93 is set to be the same as the neutral temperature at the inner boundary, given frequent 94 collisions between neutral particles and plasma. The 60° harmonic expansion developed 95 by *Arkani-Hamed* [2001] is incorporated into the MF-MHD model to take into account 96 the crustal fields. 97

98 The simulation domain is within  $-24R_M \leq X \leq 8R_M$ ;  $-16R_M \leq Y, Z \leq 16R_M$ , in 99 a nonuniform spherical grid structure with a radial resolution varying from 5 km near 100 the inner boundary to 1000 km near the outer boundary with an angular resolution of 101  $1.5^\circ - 3.0^\circ$ .  $R_M$  is the Mars radius and the results of this study are shown in the Mars- 102 centered Solar Orbital (MSO) coordinates, with x axis pointing at the Sun, y axis opposite 103 to the Mars orbital direction, and z axis perpendicular to the Mars orbital plane. The 104 neutral atmosphere is adopted from the Mars Global Ionosphere Thermosphere Model 105 (M-GITM) [*Bougher et al.*, 2015] for the cold neutral component and from the Mars 106 exosphere Monte Carlo model Adaptive Mesh Particle Simulator (M-AMPS) [*Lee et al.*, 107 2014a, b, 2015] for the hot neutral corona.

108 For this study, we have chosen the solar maximum ( $F_{10.7} = 200$  sfu), perihelion condi- 109 tions with the subsolar longitude set to  $180^\circ W$  (strong crustal field regions on the dayside) 110 to explore the boundaries. The solar wind inputs are specified as follows: a density of 4 111  $cm^{-3}$ , a plasma temperature of  $3.5 \times 10^5$  K, a velocity of 400 km/s, and the interplanetary 112 magnetic field (IMF) being 3 nT in a typical away-sector (IMF pointing away from the

113 Sun) Parker spiral pattern with an angle of  $56^\circ$ . These inputs correspond to Case 17 of  
114 *Dong et al.* [2015a].

### 3. Pressure Boundary

115 In the Mars plasma environment, the total pressure consists of three terms: magnetic  
116 pressure, dynamic pressure, and thermal pressure. These three pressures from the MF-  
117 MHD run are shown in the three rows, respectively, in Figure 1 and the three columns  
118 planar cuts  $Z=0$ ,  $X=-1.5 R_M$ , and  $X=-3 R_M$  in MSO coordinates. Typical structures of  
119 the interaction between an unmagnetized planet and the solar wind can be identified in the  
120  $Z=0$  plane. The bow shock is located  $\sim 1.7 R_M$  at the subsolar point, upstream of which  
121 the solar wind dynamic pressure dominates. After the bow shock, most (not all) of the  
122 dynamic pressure is converted into thermal and magnetic pressure, with thermal pressure  
123 prevailing near the subsolar region, and dynamic pressure progressively more important  
124 in the flanks. Closer to the planet, magnetic pressure accounts for a larger fraction of the  
125 total pressure because of mass loading effects and localized crustal fields. For  $X < 0$ , the  
126 dynamic pressure dominates the magnetosheath once behind the obstacle. In the central  
127 plasma sheet, the thermal pressure dominates the near Mars region ( $-5 < X < 0$ ) and  
128 the dynamic pressure prevails in the distant tail ( $X < -5$ ). Complementing the plasma  
129 pressure at  $X < 0$ , high magnetic pressures highlight two magnetic lobes, separated by  
130 the central plasma sheet. The magnetic pressure differs significantly when comparing the  
131 parallel and perpendicular regions (IMF parallel and perpendicular to the shock normal,  
132 respectively) of the shock as shown in Figures 1a-1c: on the more perpendicular side of  
133 the shock (+Y), there is a prominent increase in magnetic pressure, which is not present  
134 on the more parallel side of the shock (-Y). Pressures are also shown in the two selected

cuts down tail,  $X=-1.5 R_M$  and  $X=-3.0 R_M$ , where two magnetic lobe structures can be easily identified.

To help distinguish the different pressure regimes, we calculate the plasma beta ( $\beta = p_{th}/p_B$ ), i.e., the ratio of the plasma thermal pressure ( $p_{th}$ ) and the magnetic pressure ( $p_B$ ), which is shown in Figures 2a-2c, at  $Z=0$ ,  $X=-1.5 R_M$ , and  $X=-3 R_M$ , respectively. However, the plasma dynamic pressure increases downstream of the planet, as seen in Figures 1d-II. Hence, we define  $\beta^* = (p_{th} + p_{dyn})/p_B$ , which is the sum of the plasma thermal pressure ( $p_{th}$ ) and dynamic pressure ( $p_{dyn}$ ) divided by the magnetic pressure ( $p_B$ ). In other words, if  $\beta^* > 1$ , the region is dominated by the plasma-type pressures, or vice versa. Figures 2d-f illustrate the distribution of  $\beta^*$  at the three cuts. The blue color highlights regions dominated by the magnetic pressures while the red shading reveals areas dominated by the plasma-type pressures, with the white showing parity. Overall,  $\beta$  and  $\beta^*$  depict a similar pattern, with the magnetic pressure dominating the two lobes and near the planet on the dayside, and plasma-type pressures prevail in the plasma sheet, magnetosheath and beyond. The main difference is that,  $\beta^*$  defines a smaller magnetic dominant region, as the numerator includes two pressure terms. To show this more clearly, Figures 3a and 3b illustrate the contours of  $\beta = 1$  and  $\beta^* = 1$ , respectively. The view in both panels of Figure 3 is from above the ecliptic plane in the afternoon sector. The green translucent surface shows the unity contour. For reference of scale, the inner, almost spherical surface is in the ionosphere near the inner boundary of the simulation domain. Both unity contours enclose the tail lobes but the  $\beta$ -unity contour has a larger extent and extends more than  $10 R_M$  downstream of the planet.



157 Another way to identify pressure boundaries is to compute the gradients of  $\beta$  and  $\beta^*$ .  
 158 Figure 4 shows the gradient of the logarithm of  $\beta$  (a-c) and  $\beta^*$  (d-f). The gradient is  
 159 calculated along the radial direction in each plane. For the two X cuts, it is appropriate  
 160 to assume small gradients along the X direction. For the Z=0 plane, however, such a  
 161 radial gradient ( $r = \sqrt{X^2 + Y^2}$ ) is less suitable far down the tail because the gradient  
 162 should be primarily in the cylindrical radial direction, i.e. in the  $|Y|$  direction for this  
 163 plane. Hence, we should focus more on the dayside for the gradients on the Z=0 plane.  
 164 Also note that the color bars are in different ranges for three planes. As we can see, the  
 165 strong gradient layers for betas are thin on the dayside, becoming increasingly thicker and  
 166 more subdued with distance downstream of the planet. The thickness of the boundary  
 167 layer in the tail is of  $1 - 1.5 R_M$ . In addition, the unity boundaries of both  $\beta$  and  $\beta^*$   
 168 (black crosses) are coincident with the strong gradient layers (the dark red region where  
 169 the value is greater than one, indicating an order of magnitude change per  $R_M$ ). On  
 170 the other hand, even though the unity contour extends to large distances down the tail  
 171 ( $> 10R_M$ ), the transition becomes too gradual, as indicated by the large area colored  
 172 white in Figures 2a and 2d for  $X < -4 R_M$ , to be a meaningful boundary indicator. In  
 173 addition, the grid resolution is rather coarse in the far tail. Hence, we only select y-z  
 174 planar cuts as far as  $3 R_M$  down tail.

#### 4. Ion Composition Boundary

175 As mentioned above, four ion species,  $H^+$ ,  $O^+$ ,  $O_2^+$ , and  $CO_2^+$ , are included in the  
 176 simulation. Figure 5 shows the  $H^+$  mass (also number) density, the heavy ion ( $CO_2^+$ ,  $O^+$ ,  
 177 and  $O_2^+$ ) mass density, and the heavy ion number density from the MF-MHD model in the  
 178 three rows, respectively. The three columns again are for Z=0, X=-1.5  $R_M$ , and X=-3

179  $R_M$  cuts.  $H^+$  dominates the sheath and beyond (Figures 5a-5c), and high  $H^+$  density is  
 180 also seen near the planet (Figures 5a and 5b), of a planetary origin as the density is too  
 181 high to be solar wind originated. High heavy ion density is seen near the planet as well  
 182 as the central plasma sheet, as expected. Further down the tail, the heavy ion escape is  
 183 more concentrated in the plasma central sheet, as seen by comparing Figures 5e and 5h  
 184 with Figures 5j and 5i. The energetic loss plume due to pick up ions by the convective  
 185 electric field carried by the solar wind ( $\mathbf{E} = -\mathbf{U} \times \mathbf{B}$ ) is also seen in Figures 5e, 5f, 5h,  
 186 and 5i, oriented in the +Z direction due to the +By component of the input IMF, but  
 187 less prominent in the number density figures.

188 To define a model-based ion composition boundary, we calculate the ratio of the  $H^+$   
 189 density and the heavy ion density, for both mass density and number density. The results  
 190 for the aforementioned three cuts are shown in Figure 6, the first row for the mass density  
 191 ratio and the second row for the number density ratio. An interesting finding is that the  
 192 white color, indicating a ratio of 1, encloses both the plasma sheet and the magnetic lobes,  
 193 indicating that both regions are dominated by planetary heavy ions. Again, for  $X < -4$   
 194  $R_M$ , the transition from  $H^+$  to heavy ions becomes less distinct with increasing distance  
 195 down the tail.

196 Figure 7 shows the unity contours for the mass density ratio (a) and the number density  
 197 ratio (b). The view is from slightly above the ecliptic plane and slightly sunward of the  
 198 dusk terminator. Both unity boundaries extend very far down the tail ( $> 10R_M$ ) and  
 199 also overlap with the magnetic lobes. The mass density unity contour is larger than the  
 200 number density ratio unity contour because it has a mass multiplier. Also, the plume is

201 more prominent and extended for the mass density ratio unity contour but barely seen in  
 202 the number density ratio unity contour.

203 In a similar fashion, the gradients of the logarithms of the density ratios are also cal-  
 204 culated, shown in Figure 8, a-c for the mass density ratio and d-f for the number density  
 205 ratio. The gradients are computed in the same way as the betas. Again, thin and sharp  
 206 strong gradient layers are seen on the dayside (Figures 8a and 8d), and also coincide with  
 207 the unity boundaries, marked by the black crosses. In the tail (Figures 8b, 8c, 8e, and  
 208 8f), the strong gradient layers, again, are of a thickness of  $1 - 1.5 R_M$ , similar to Figure 4,  
 209 and become thicker further down tail, comparing Figure 8b with 8c and Figure 8e with 8f.  
 210 Furthermore, the gradients are about the same for the mass density ratio and the number  
 211 density ratio as the mass multiplier is mostly cancelled from the logarithmic gradient cal-  
 212 culation. With that as a reference, the unity of the mass density ratio, naturally larger,  
 213 marks the center of the strong gradient layer while the unity of the number density ratio  
 214 is more closely aligned with the inner edge.

## 5. Comparisons

215 Now that we have defined model-based pressure and composition boundaries, resembling  
 216 the observationally based magnetic pileup and ion composition boundaries, the next step  
 217 is to compare these boundaries. Figure 9 shows the comparisons between the pressure  
 218 boundary and the ion composition boundary via different methods. The three columns are  
 219 for  $Z = 0$  (Figures 9a, 9d, and 9g),  $X = -1.5 R_M$  (Figures 9b, 9e, and 9h), and  $X = -3$   
 220  $R_M$  (Figures 9c, 9f, and 9i). The first row shows the unities of  $\beta$ ,  $\beta^*$ , ion mass density  
 221 ratio, and ion number density ratio, colored in black, blue, green, and red, respectively.  
 222 For the equatorial plane, we have zoomed in to focus on the dayside. The unity contours

223 for these four quantities are basically on top of each other and exhibit asymmetry about  
 224 the X axis probably due to the effects of quasi-parallel and quasi-perpendicular shocks  
 225 (see Figure 1a). The two betas also have another inner unity curve, a balance between the  
 226 ionospheric plasma-type pressure and the magnetic pressure. For the tail cuts, the unities  
 227 of  $\beta$ ,  $\beta^*$ , and ion mass density ratio mostly coincide on the outer edge at  $X = -1.5$   
 228  $R_M$ , while the ion number density ratio unity is systematically smaller. Further down  
 229 tail, at  $X = -3R_M$  (Figure 9c), the  $\beta$  unity is the outmost, then slightly inward are the  
 230 overlapping  $\beta^*$  and ion mass density ratio unities, and ion number density ratio unity is  
 231 located as the innermost curve.

232 Upstream of the planet ( $X > 0$ ) along the Mars-Sun line (Figure 9d, leftmost column),  
 233 transitions in the pressure and density ratios are apparent at the bow shock ( $X=1.75$ ) and  
 234 near the MPB ( $X = 1.2 - 1.3$ ). Downstream of the planet ( $X < 0$ ), the unities begin to  
 235 separate along Y with distance down tail as the transition from plasma-type pressure and  
 236  $H^+$  dominance to magnetic pressure and heavy ions dominance becomes more gradual, as  
 237 shown in the right two columns of Figures 9. Each quantity has sharper transitions closer  
 238 to the planet.

239 To better compare the locations of unities with the locations of maximum gradient  
 240 in the various quantities, the bottom row shows the gradient of the logarithmic values  
 241 along the Mars-Sun line (Figure 9g) and in the cross-tail Y direction at  $X = -1.5$  and  
 242  $X = -3$  (Figure 9h and 9i), with color-coded vertical dashed lines marking the innermost  
 243 and outermost unity locations. The maximum gradients of the four quantities are nearly  
 244 co-located. The tailward magnetosheath ( $2.5 < |Y| < 4R_M$ , and  $-3 < |Y| < -1.5R_M$   
 245 approximately) is a region dominated by  $H^+$  (density ratio  $\gg 1$ ) and dynamic pressure

246 ( $\beta^* \gg \beta$ ). At the inner edge of this region ( $|Y| \sim 2 - 2.5R_M$ ), the composition and all of  
 247 the pressure terms exhibit sharp gradients at nearly the same location (right two columns  
 248 of Fig. 9), suggesting that all mark the same physical transition. Third, gradient extrema  
 249 agree very well with the unities of  $\beta$ ,  $\beta^*$ , and ion mass density ratio, while the ion number  
 250 density unity is located systematically inward of the gradient extrema (Figure 8 and  
 251 Figure 9). Thus, the unities in  $\beta$ ,  $\beta^*$ , and mass density ratio provide convenient proxies  
 252 for the boundaries between distinct regions of the Mars plasma environment. This also  
 253 shows that the same physical boundary may be identified using different measurement  
 254 techniques.

255 Along the Mars-Sun line (Figure 9g), a strong gradient layer for all quantities is seen at  
 256 the bow shock ( $X \sim 1.7 R_M$ ) with a thickness of about  $0.1 R_M$  (300–400 km). Downstream  
 257 of the bow shock, near  $1.25 R_M$ , a positive gradient layer for  $\beta$  and  $\beta^*$  (nearly identical  
 258 due to a negligible dynamic pressure) is seen with a thickness of  $\sim 0.1 R_M$ . The behavior  
 259 of the ion density ratio near  $1.25 R_M$  is slightly different. Both the mass and number  
 260 density ratios are positive, primarily because the heavy ion density decreases  
 261 with altitude. However, the ion mass and number density unities are clearly offset from  
 262 the beta unity by  $\sim 0.05 R_M$  (Fig. 9d). To further examine this region, Figure 10 depicts  
 263 the heavy ion mass density (black),  $H^+$  density (blue), and the ratio of the two (red)  
 264 along the Mars-Sun line (MSO X axis). Moving inward from the bow shock towards the  
 265 planet, the heavy ion mass density increases with decreasing altitude, slowly at first, then  
 266 more rapidly as the mass density unity is approached. Interior to the unity, the heavy  
 267 ion mass density rises steeply and soon dominates the total mass density. Meanwhile,  
 268 the proton density remains nearly constant until the unity is reached, and then drops

269 gradually by a factor of  $\sim 3$ . The inflection in the heavy ion mass density from 1.2 to  
270  $1.35 R_M$  corresponds to the dips of the ion density ratio gradients (Figure 9g), which  
271 are nearly co-located with strong beta gradients. This feature could be explained by an  
272 increase in ion production due to the electron impact ionization and charge exchange near  
273 the MPR [e.g. *Crider et al., 2000; Jin et al., 2006*] as well as the compression of planetary  
274 plasma by the solar wind. If we take the ion composition boundary to be centered on the  
275 mass density unity, then its thickness, as defined by the heavy ion mass density inflection,  
276 would be  $\sim 0.1 R_M$ .

## 6. Discussion and Conclusions

277 This study quantitatively examined pressure and composition transitions in the Mars-  
278 solar wind interaction region by calculating gradients and unities of plasma  $\beta$  and  $\beta^*$ ,  
279 as well as ion mass and number density ratios. We found that the unity contours are  
280 nearly co-located with the gradient extrema, so that they may be conveniently used to  
281 define physical boundaries in the system. Historically, these pressure and composition  
282 transitions have mostly been simplified as sharp, cylindrically symmetric boundaries. In  
283 this study, the unity contours and gradients of betas and ion density ratios have shown  
284 that these boundaries are structured and have a finite thickness, ranging from  $0.05 - 0.1$   
285  $R_M$  near the sub-solar region to  $1 - 1.5 R_M$  in the tail. The unity contours enclose  
286 magnetic lobes filled with planetary heavy ions to more than  $10 R_M$  down tail. The  
287 pressure and composition gradients get progressively weaker and broader with increasing  
288 distance down the tail, presumably becoming indiscernible at large distances downstream.  
289 With a comprehensive set of instruments to measure the near Martian space environment,  
290 MAVEN data are being used to study these boundaries in detail [e.g. *Matsunaga et al.,*

291 2015]. The boundary shape and structure presented here can provide physical insight for  
292 these observational studies.

293 We examined the relationship between pressure and composition boundaries (corre-  
294 sponding to the observationally based MPB and ICB, respectively) by comparing unities  
295 and gradients of two betas and two ion density ratios. The unities are nearly co-located  
296 (Figure 9), it is easy to see that the unities mostly match with each other, except for the  
297 ion number density ratio unity, which is systematically interior to other unity boundaries.  
298 In the tail, the locations of the pressure and composition boundaries are very similar,  
299 which means the planetary heavy ions dominate not only the central plasma sheet but  
300 also the magnetic lobes. Even though heavy ions are more concentrated near the plasma  
301 sheet, the magnetic lobes are devoid of  $H^+$  so that heavy ions still prevail. This means  
302 that ion escape down the tail occurs in both the plasma sheet and across the much larger  
303 cross sectional area of the magnetic lobes. Downstream of the bow shock, Figure 10 shows  
304 that the decrease of solar wind proton density does not begin until the mass density ratio  
305 reaches unity. In addition, the model suggests that the ion composition boundary is struc-  
306 tured, as revealed by an inflection in the heavy ion mass density gradient, which may be  
307 associated with enhanced electron impact ionization and charge exchange in this region.

308 While observationally, the MPB and ICB seem to occur close to one another, especially  
309 for  $X > 0$ , it has been unclear how these two boundaries are associated physically. In  
310 the tail region, the MF-MHD simulation exhibits a sharp outer edge to the lobes at the  
311 same location in both composition and beta. Magnetic field lines in the lobes are draped  
312 closely by Mars' upper atmosphere, and may in some cases be connected to planetary  
313 crustal fields. The ionosphere could then plausibly provide the source of planetary ions in

314 the lobes. The composition and pressure boundaries deviate from one another in the tail  
315 near the  $Y = 0$  plane for several reasons. First, there is a dense plasma sheet of planetary  
316 ions that dominates the pressure between the lobes. Second, there is an energetic plume  
317 of planetary ions in the  $+Z$  direction that have very large gyroradii and move differently  
318 than the magnetic field. Third, the convection electric field accelerates planetary ions  
319 in the  $-Z$  hemisphere back into the central tail region, which creates a small outward  
320 extension of the composition boundary in that direction (seen in Figure 9b and 9c).

321 The comparison between the boundaries determined from a MF-MHD simulation with  
322 the analytical fittings of MPB from *Vignes et al.* [2000] (based on MGS observations only)  
323 and *Trotignon et al.* [2006] (the combination of Pbobos-2 and MGS observations) is shown  
324 in Figures 4a, 4d, 8a, and 8d. The two fits are highlighted in green solid line and red  
325 dashed line, respectively. In the tail, it is easy to see that the unity boundaries, except for  
326 the ion number density ratio presented in this study, match with the Vignes fitting and  
327 show little flaring, in contrast to a large flaring angle from the Trotignon fitting. The unity  
328 contour of the ion number density ratio, in fact, moves inward (towards the X axis) with  
329 distance down the tail, so the shape of this boundary depends on how it is defined. On  
330 the dayside, unity boundaries in this study are mostly located outside both fits, especially  
331 at higher solar zenith angle, and also exhibit a dawn-dusk asymmetry, probably due to  
332 the different in shock geometries (quasi-parallel vs. quasi-perpendicular) at the dawn and  
333 dusk sides. Existing data show a large spread of MPB locations at the tail [*Vignes et al.*,  
334 2000], which can be attributed to many factors, such as the different upstream conditions  
335 and different locations of strong crustal magnetic fields with respect to the sub-solar point.



336 However, it might also be partially due to the structure and asymmetry of this boundary,  
337 which have so far not been considered in observational studies.

338 Finally, this study focuses on the three dimensional shape and structure of the pressure  
339 and composition boundaries, which can be used as theoretical guidance for observational  
340 analyses. In particular, MAVEN data is now being used to study these boundaries in  
341 details [e.g. *Matsunaga et al.*, 2015]. Future work with a suite of MF-MHD models will  
342 investigate how the upstream conditions, strong crustal field locations, neutral atmosphere  
343 and ionosphere affect these boundaries.

344 **Acknowledgments.** The authors would like to thank NASA for support of this project  
345 under grants NNX13AG26G and NNS14AH19G. The authors also thank support from  
346 the NASA Mars Scout Program. The authors thank Zhenguang Huang and Judit Szenté  
347 for teaching S. Xu Tecplot, which makes this study possible. The BATS-R-US code is  
348 publicly available from <http://csem.engin.umich.edu/tools/swmf>. For distribution of the  
349 model results used in this study, please contact C. Dong ([dcfy@pppl.gov](mailto:dcfy@pppl.gov)).

## References

- 350 Acuna, M., J. Connerney, R. Lin, D. Mitchell, C. Carlson, J. McFadden, K. Anderson,  
351 H. Rème, C. Mazelle, D. Vignes, et al. (1999), Global distribution of crustal magneti-  
352 zation discovered by the mars global surveyor mag/er experiment, *Science*, *284*(5415),  
353 790–793.
- 354 Arkani-Hamed, J. (2001), A 50-degree spherical harmonic model of the magnetic field of  
355 mars, *Journal of Geophysical Research: Planets (1991–2012)*, *106*(E10), 23,197–23,208.

- 356 Bertucci, C., C. Mazelle, M. Acuna, C. Russell, and J. Slavin (2005), Structure of the  
357 magnetic pileup boundary at mars and venus, *Journal of Geophysical Research: Space*  
358 *Physics (1978–2012)*, 110(A1).
- 359 Bertucci, C., F. Duru, N. Edberg, M. Fraenz, C. Martinecz, K. Szego, and O. Vaisberg  
360 (2012), The induced magnetospheres of mars, venus, and titan, in *The Plasma Envi-*  
361 *ronment of Venus, Mars, and Titan*, pp. 113–171, Springer.
- 362 Bößwetter, A., T. Bagdonat, U. Motschmann, and K. Sauer (2004), Plasma bound-  
363 aries at mars: a 3-d simulation study, *Annales Geophysicae*, 22(12), 4363–4379, doi:  
364 10.5194/angeo-22-4363-2004.
- 365 Bougher, S., D. Pawlowski, J. Bell, S. Nelli, T. McDunn, J. Murphy, M. Chizek, and  
366 A. Ridley (2015), Mars global ionosphere-thermosphere model: Solar cycle, seasonal,  
367 and diurnal variations of the mars upper atmosphere, *Journal of Geophysical Research:*  
368 *Planets*, 120(2), 311–342.
- 369 Brain, D., F. Bagenal, M. Acuña, and J. Connerney (2003), Martian magnetic morphol-  
370 ogy: Contributions from the solar wind and crust, *Journal of Geophysical Research:*  
371 *Space Physics (1978–2012)*, 108(A12).
- 372 Brain, D., R. Lillis, D. Mitchell, J. Halekas, and R. Lin (2007), Electron pitch angle  
373 distributions as indicators of magnetic field topology near mars, *Journal of Geophysical*  
374 *Research: Space Physics (1978–2012)*, 112(A9).
- 375 Brain, D., S. Barabash, A. Boesswetter, S. Bougher, S. Brecht, G. Chanteur, D. Hur-  
376 ley, E. Dubinin, X. Fang, M. Fraenz, J. Halekas, E. Harnett, M. Holmstrom, E. Kallio,  
377 H. Lammer, S. Ledvina, M. Liemohn, K. Liu, J. Luhmann, Y. Ma, R. Modolo, A. Nagy,  
378 U. Motschmann, H. Nilsson, H. Shinagawa, S. Simon, and N. Terada (2010), A compar-

379 ison of global models for the solar wind interaction with Mars, *ICARUS*, *206*, 139–151,  
380 doi:10.1016/j.icarus.2009.06.030.

381 Brecht, S. H. (1990), Magnetic asymmetries of unmagnetized planets, *Geophysical Re-*  
382 *search Letters*, *17*, 1243–1246, doi:10.1029/GL017i009p01243.

383 Brecht, S. H. (1997), Hybrid simulations of the magnetic topology of Mars, *Journal of*  
384 *Geophysical Research: Space Physics*, *102*, 4743–4750, doi:10.1029/96JA03205.

385 Connerney, J., J. Espley, R. Oliverson, D. Sheppard, and G. Dibraccio (2015), First  
386 results from the maven magnetic field investigation, in *Lunar and Planetary Science*  
387 *Conference*, vol. 46, p. 1080.

388 Cravens, T., J. Kozyra, A. Nagy, T. Gombosi, and M. Kurtz (1987), Electron impact  
389 ionization in the vicinity of comets, *Journal of Geophysical Research: Space Physics*  
390 *(1978–2012)*, *92*(A7), 7341–7353.

391 Crider, D. H., Cloutier, C. Law, P. Walker, Y. Chen, M. Acua, J. Connerney, D. Mitchell,  
392 R. Lin, K. Anderson, C. Carlson, J. McFadden, H. Rme, C. Mazelle, C. d’Uston,  
393 J. Sauval, D. Vignes, D. Brain, and N. Ness (2000), Evidence of electron impact ion-  
394 ization in the magnetic pileup boundary of mars, *Geophysical Research Letters*, *27*(1),  
395 45–48, doi:10.1029/1999GL003625.

396 Crider, D. H., M. H. Acuña, J. E. P. Connerney, D. Vignes, N. F. Ness, A. M. Krymskii,  
397 T. K. Breus, H. Rème, C. Mazelle, D. L. Mitchell, R. P. Lin, P. A. Cloutier, and  
398 D. Winterhalter (2002), Observations of the latitude dependence of the location of  
399 the martian magnetic pileup boundary, *Geophysical Research Letters*, *29*, 1170, doi:  
400 10.1029/2001GL013860.

- 401 Dong, C., S. W. Bougher, Y. Ma, G. Toth, A. F. Nagy, and D. Najib (2014), Solar wind  
402 interaction with mars upper atmosphere: Results from the one-way coupling between  
403 the multifluid mhd model and the mtgcm model, *Geophysical Research Letters*, *41*(8),  
404 2708–2715.
- 405 Dong, C., S. W. Bougher, Y. Ma, G. Toth, Y. Lee, A. F. Nagy, V. Tenishev, D. J.  
406 Pawlowski, M. R. Combi, and D. Najib (2015a), Solar wind interaction with the martian  
407 upper atmosphere: Crustal field orientation, solar cycle, and seasonal variations, *Journal*  
408 *of Geophysical Research: Space Physics*, *120*(9), 7857–7872, doi:10.1002/2015JA020990,  
409 2015JA020990.
- 410 Dong, C., Y. Ma, S. W. Bougher, G. Toth, A. F. Nagy, J. S. Halekas, Y. Dong, S. M.  
411 Curry, J. G. Luhmann, D. Brain, et al. (2015b), Multifluid mhd study of the solar  
412 wind interaction with mars' upper atmosphere during the 2015 march 8th icme event,  
413 *Geophysical Research Letters*, *42*(21), 9103–9112.
- 414 Dubinin, E., M. Fränz, J. Woch, E. Roussos, S. Barabash, R. Lundin, J. Winningham,  
415 R. Fraenz, and M. Acuña (2006), Plasma morphology at mars. aspera-3 observations,  
416 *Space Science Reviews*, *126*(1-4), 209–238.
- 417 Dubinin, E., R. Modolo, M. Fraenz, J. Woch, F. Duru, F. Akalin, D. Gurnett,  
418 R. Lundin, S. Barabash, J. Plaut, et al. (2008), Structure and dynamics of the so-  
419 lar wind/ionosphere interface on mars: Mex-aspera-3 and mex-marsis observations,  
420 *Geophysical Research Letters*, *35*(11).
- 421 Fang, X., Y. Ma, D. Brain, Y. Dong, and R. Lillis (2015), Control of mars global atmo-  
422 spheric loss by the continuous rotation of the crustal magnetic field: A time-dependent  
423 mhd study, *Journal of Geophysical Research: Space Physics*, *120*(12), 10,926–10,944,

- 424 doi:10.1002/2015JA021605, 2015JA021605.
- 425 Fränz, M., E. Dubinin, E. Roussos, J. Woch, J. Winningham, R. Frahm, A. Coates,  
426 A. Fedorov, S. Barabash, and R. Lundin (2006), Plasma moments in the environment  
427 of mars, *Space Science Reviews*, 126(1-4), 165–207.
- 428 Glocer, A. C. Fth, Y. Ma, T. Gombosi, J.-C. Zhang, and L. M. Kistler (2009), Multifluid  
429 block-adaptive-tree solar wind roe-type upwind scheme: Magnetospheric composition  
430 and dynamics during geomagnetic storms?initial results, *Journal of Geophysical Re-*  
431 *search: Space Physics*, 114(A12), n/a–n/a, doi:10.1029/2009JA014418, a12203.
- 432 Halekas, J., J. McFadden, J. Connerney, J. Espley, D. Brain, D. Mitchell, D. Larson,  
433 Y. Harada, T. Hara, S. Ruhunusiri, et al. (2015), Time-dispersed ion signatures observed  
434 in the martian magnetosphere by maven, *Geophysical Research Letters*, 42(21), 8910–  
435 8916.
- 436 Harnett, F. M. and R. M. Winglee (2005), Three-dimensional fluid simulations of plasma  
437 asymmetries in the martian magnetotail caused by the magnetic anomalies, *Journal of*  
438 *Geophysical Research: Space Physics*, 110(A7), n/a–n/a, doi:10.1029/2003JA010315.
- 439 Jakosky, B. M., R. Lin, J. Grebowsky, J. Luhmann, D. Mitchell, G. Beutelschies, T. Priser,  
440 M. Acuna, I. Andersson, D. Baird, et al. (2015a), The mars atmosphere and volatile  
441 evolution (maven) mission, *Space Science Reviews*, pp. 1–46.
- 442 Jakosky, B. M., J. M. Grebowsky, J. G. Luhmann, J. Connerney, F. Eparvier, R. Ergun,  
443 J. Halekas, D. Larson, P. Mahaffy, J. Mcfadden, et al. (2015b), Maven observations of  
444 the response of mars to an interplanetary coronal mass ejection, *Science*, 350(6261),  
445 aad0210.

- 446 Jin, H., K. Maezawa, and T. Mukai (2006), Effects of charge exchange and electron  
447 impact ionization on the formation of the magnetic pileup boundary at mars, *Journal*  
448 *of Geophysical Research: Space Physics (1978–2012)*, *111*(A5).
- 449 Kallio, E., A. Fedorov, E. Budnik, T. Säles, P. Janhunen, W. Schmidt, H. Koskinen,  
450 P. Riihelä, S. Barabash, R. Lundin, M. Holmström, H. Gunell, K. Brinkfeldt, Y. Fu-  
451 taana, H. Andersson, M. Yamauchi, A. Grigoriev, J.-A. Sauvaud, J.-J. Thocaven, J. D.  
452 Winningham, R. A. Frahm, J. R. Sharber, J. R. Scherrer, A. J. Coates, D. R. Linder,  
453 D. O. Katarina, J. Kozyra, J. G. Luhmann, E. Roelof, D. Williams, S. Livi, C. C. Curtis,  
454 K. C. Hsieh, B. R. Sandel, M. Grande, M. Carter, S. McKenna-Lawler, S. Orsini,  
455 R. Cerulli-Irelli, M. Maggi, P. Wurz, P. Bochsler, N. Krupp, J. Woch, M. Fränz,  
456 K. Asamura, and C. Dierker (2006), Ion escape at Mars: Comparison of a 3-D hybrid  
457 simulation with Mars Express IMA/ASPERA-3 measurements, *ICARUS*, *182*, 350–359,  
458 doi:10.1016/j.icarus.2005.09.018.
- 459 Lee, Y., M. R. Combi, V. Tennishev, and S. W. Bougher (2014a), Hot carbon corona in  
460 mars' upper thermosphere and exosphere: 1. mechanisms and structure of the hot  
461 corona for low solar activity at equinox, *Journal of Geophysical Research: Planets*,  
462 *119*(5), 905–924.
- 463 Lee, Y., M. R. Combi, V. Tennishev, and S. W. Bougher (2014b), Hot carbon corona in  
464 mars' upper thermosphere and exosphere: 2. solar cycle and seasonal variability, *Journal*  
465 *of Geophysical Research: Planets*, *119*(12), 2487–2509.
- 466 Lee, Y., M. R. Combi, V. Tennishev, S. W. Bougher, and R. J. Lillis (2015), Hot oxygen  
467 corona at mars and the photochemical escape of oxygen: Improved description of the  
468 thermosphere, ionosphere, and exosphere, *Journal of Geophysical Research: Planets*,

- 469 120(11), 1880–1892.
- 470 Liemohn, M. W., Y. Ma, R. A. Frahm, X. Fang, J. U. Kozyra, A. F. Nagy, J. D. Winning-  
471 ham, J. R. Sharber, S. Barabash, and R. Lundin (2006), Mars Global MHD Predictions  
472 of Magnetic Connectivity Between the Dayside Ionosphere and the Magnetospheric  
473 Flanks, *Space Science Reviews*, 126, 63–76, doi:10.1007/s11214-006-9116-8.
- 474 Liemohn, M. W., Y. Ma, A. Nagy, J. Kozyra, J. Winningham, R. Frahm, J. Sharber,  
475 S. Barabash, and R. Lundin (2007), Numerical modeling of the magnetic topology near  
476 mars auroral observations, *Geophysical Research Letters*, 34(24).
- 477 Ma, Y., A. F. Nagy, K. C. Hansen, D. L. DeZeeuw, T. I. Gombosi, and K. Powell (2002),  
478 Three-dimensional multispecies mhd studies of the solar wind interaction with mars in  
479 the presence of crustal fields, *Journal of Geophysical Research: Space Physics (1978–*  
480 *2012)*, 107(A10), 1282–1289.
- 481 Ma, Y., A. F. Nagy, I. V. Sokolov, and K. C. Hansen (2004), Three-dimensional, mul-  
482 tispecies high spatial resolution mhd studies of the solar wind interaction with mars,  
483 *Journal of Geophysical Research: Space Physics (1978–2012)*, 109(A7).
- 484 Ma, Y., X. Fang, C. T. Russell, A. F. Nagy, G. Toth, J. G. Luhmann, D. A. Brain, and  
485 C. Dong (2014), Effects of crustal field rotation on the solar wind plasma interaction  
486 with mars, *Geophysical Research Letters*, 41(19), 6563–6569.
- 487 Ma, Y., C. Russell, X. Fang, Y. Dong, A. Nagy, G. Toth, J. Halekas, J. Connerney,  
488 J. Espley, P. Mahaffy, et al. (2015), Mhd model results of solar wind interaction with  
489 mars and comparison with maven plasma observations, *Geophysical Research Letters*,  
490 42(21), 9113–9120.

- 491 Matsunaga, K., et al. (2015), Comparison of martian magnetic pileup boundary with ion  
492 composition boundary observed by maven, *AGU Fall Meeting, Abstract P21A-2071*.
- 493 Modolo, R., G. M. Chanteur, E. Dubinin, and A. P. Matthews (2006), Simulated solar  
494 wind plasma interaction with the Martian exosphere: influence of the solar EUV flux on  
495 the bow shock and the magnetic pile-up boundary, *Annales Geophysicae*, *24*, 3403–3410,  
496 doi:10.5194/angeo-24-3403-2006.
- 497 Moore, T., and D. Delcourt (1995), The geopause, *Reviews of Geophysics*, *33*(2), 175–209.
- 498 Nagy, A., D. Winterhalter, K. Sauer, T. Cravens, S. Brecht, C. Mazelle, D. Crider,  
499 E. Kallio, A. Zakharov, E. Dubinin, et al. (2004), The plasma environment of mars,  
500 in *Mars? Magnetism and Its Interaction with the Solar Wind*, pp. 33–114, Springer.
- 501 Najib, D., A. F. Nagy, G. Tóth, and Y. Ma (2011), Three-dimensional, multifluid, high  
502 spatial resolution mhd model studies of the solar wind interaction with mars, *Journal*  
503 *of Geophysical Research: Space Physics (1978–2012)*, *116*(A5).
- 504 Powell, K. G., P. L. Roe, T. J. Linde, T. I. Gombosi, and D. L. De Zeeuw (1999), A  
505 Solution Adaptive Upwind Scheme for Ideal Magnetohydrodynamics, *Journal of Com-*  
506 *putational Physics*, *154*, 284–309, doi:10.1006/jcph.1999.6299.
- 507 Riedler, W., B. Möhlmann, V. Oraevsky, K. Schwingenschuh, Y. Yeroshenko, J. Rusten-  
508 bach, O. Avdogar, G. Berghofer, H. Lichtenegger, M. Delva, et al. (1989), Magnetic  
509 fields near mars: first results, *Nature*, *341*(6243), 604–607.
- 510 Sauer, K., T. Roatsch, U. Motschmann, K. Schwingenschuh, R. Lundin, H. Rosenbauer,  
511 and S. Livi (1992), Observations of plasma boundaries and phenomena around mars  
512 with phobos 2, *Journal of Geophysical Research: Space Physics (1978–2012)*, *97*(A5),  
513 6227–6233.



- 514 Sauer, K., A. Bogdanov, and K. Baumgärtel (1994), Evidence of an ion composition  
515 boundary (protonopause) in bi-ion fluid simulations of solar wind mass loading, *Geo-*  
516 *physical research letters*, *21*(20), 2255–2258.
- 517 Schunk, R., and A. Nagy (2009), *Ionospheres*, Cambridge University Press.
- 518 Simon, S. A., Boeswetter, T. Bagdonat, and U. Motschmann (2007), Physics of the ion  
519 composition boundary: a comparative 3-d hybrid simulation study of mars and titan,  
520 *Annales Geophysicae*, *25*(1), 99–115, doi:10.5194/angeo-25-99-2007.
- 521 Tóth, G., B. van der Holst, I. V. Sokolov, D. L. De Zeeuw, T. I. Gombosi, F. Fang, W. B.  
522 Manchester, X. Meng, D. Najib, K. G. Powell, Q. F. Stout, A. Glocer, Y.-J. Ma, and  
523 M. Opher (2012), Adaptive numerical algorithms in space weather modeling, *Journal*  
524 *of Computational Physics*, *231*, 870–903, doi:10.1016/j.jcp.2011.02.006.
- 525 Trotignon, J. C. Mazelle, C. Bertucci, and M. Acu?a (2006), Martian shock and  
526 magnetic pile-up boundary positions and shapes determined from the phobos 2 and  
527 mars global surveyor data sets, *Planetary and Space Science*, *54*(4), 357 – 369, doi:  
528 <http://dx.doi.org/10.1016/j.pss.2006.01.003>.
- 529 Trotignon, J. G., E. Dubinin, R. Grard, S. Barabash, and R. Lundin (1996), Martian plan-  
530 etopause as seen by the plasma wave system onboard phobos 2, *Journal of Geophysical*  
531 *Research: Space Physics (1978–2012)*, *101*(A11), 24,965–24,977.
- 532 Vignes, D., C. Mazelle, H. Rme, M. H. Acuña, J. E. P. Connerney, R. P. Lin, D. L.  
533 Mitchell, P. Cloutier, D. H. Crider, and N. F. Ness (2000), The solar wind interaction  
534 with Mars: Locations and shapes of the bow shock and the magnetic pile-up boundary  
535 from the observations of the MAG/ER Experiment onboard Mars Global Surveyor,  
536 *Geophysical Research Letters*, *27*, 49–52, doi:10.1029/1999GL010703.

537 Xu, S., M. W. Liemohn, and D. L. Mitchell (2014), Solar wind electron precipita-  
538 tion into the dayside martian upper atmosphere through the cusps of strong crustal  
539 fields, *Journal of Geophysical Research: Space Physics*, 119(12), 10,100–10,115, doi:  
540 10.1002/2014JA020363.

Author Manuscript

D R A F T

June 28, 2016, 11:31pm

D R A F T

**Figure 1.** The three rows, from top to bottom, show the magnetic pressure (Pa), the dynamic pressure (Pa), and the thermal pressure (Pa), and the three columns, from left to right, are for  $Z=0$ ,  $X=-1.5 R_M$ , and  $X=-3 R_M$  in MSO coordinates. The values are logarithmic scale. The two vertical dashed lines in the first column mark the positions of the two X slices in the second and third columns.

**Figure 2.** Plasma beta ( $\beta$ ), i.e., the ratio of the plasma thermal pressure and the magnetic pressure, is shown in a-c, at  $Z=0$ ,  $X=-1.5 R_M$ , and  $X=-3 R_M$ , respectively, while  $\beta^*$ , which is the sum of the plasma thermal pressure and dynamic pressure divided by the magnetic pressure, shown in d-f, at  $Z=0$ ,  $X=-1.5 R_M$ , and  $X=-3 R_M$ , respectively. The values are logarithmic scale. The two vertical dashed lines in the first column mark the positions of the two X slices in the second and third columns.

**Figure 3.** The contours of  $\beta = 1$  (a) and  $\beta^* = 1$  (b).

**Figure 4.** The gradient of the logarithm of  $\beta$  (a-c) and  $\beta^*$  (d-f). From left to right, the three columns are for three cuts,  $Z=0$ ,  $X=-1.5 R_M$ , and  $X=-3 R_M$  in MSO coordinates. The black crosses highlight the unities of  $\beta$  and  $\beta^*$ , as extracted from Figure 2. The green solid line and red dashed line in a and d represent the MPB fitting from *Vignes et al.* [2000] and *Trotignon et al.* [1996], respectively.

**Figure 5.** The three rows, from top to bottom, show the mass density of  $H^+$  ( $\text{amu}/\text{cm}^3$ ), the mass density ( $\text{amu}/\text{cm}^3$ ) of heavy ions ( $\text{CO}_2^+$ ,  $\text{O}^+$ , and  $\text{O}_2^+$ ), and the number density ( $\text{cm}^{-3}$ ) of heavy ions, and the three columns, from left to right, are for  $Z=0$ ,  $X=-1.5 R_M$ , and  $X=-3 R_M$  in MSO coordinates. The values are logarithmic scale. The two vertical dashed lines in the first column mark the positions of the two X slices in the second and third columns.

**Figure 6.** The ratio of the mass density of  $H^+$  and heavy ions is shown in a-c, at  $Z=0$ ,  $X=-1.5 R_M$ , and  $X=-3 R_M$ , respectively, while the ratio of the number density of  $H^+$  and heavy ions is shown in d-f, at  $Z=0$ ,  $X=-1.5 R_M$ , and  $X=-3 R_M$ , respectively. The values are logarithmic scale. The two vertical dashed lines in the first column mark the positions of the two  $X$  slices in the second and third columns.

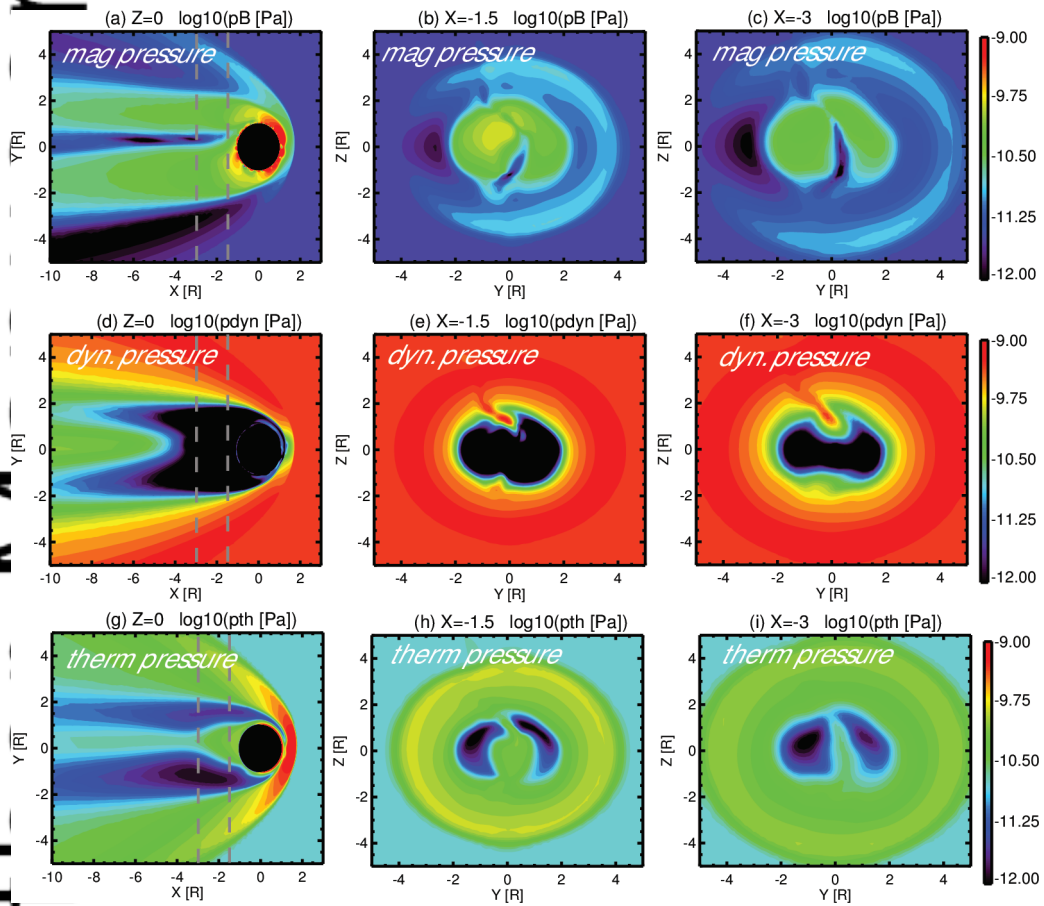
**Figure 7.** The contours of the ion mass density ratio = 1 (a) and the ion number density ratio = 1 (b).

**Figure 8.** The gradient of the logarithm of the ion mass density ratio (a-c) and the ion number density ratio (d-f). From left to right, the three columns are for three cuts,  $Z=0$ ,  $X=-1.5 R_M$ , and  $X=-3 R_M$  in MSO coordinates. The black crosses highlight the unities of the ratios, as extracted from Figure 6. The green solid line and red dashed line in a and d represent the MPB fitting from [Vignes *et al.*, 2000] and Trotignon *et al.* [2006], respectively.

**Figure 9.** Comparison of unities and gradients at  $Z=0$  (a, d, g),  $X=-1.5 R_M$  (b, e, h) and  $X=-3 R_M$  (c, f, i). The first row (a-c) shows the unities of  $\beta$ ,  $\beta^*$ , ion mass density ratio, and ion number density ratio, colored in black, blue, green, and red, respectively. The second row shows the line plots of the logarithmic values of the same four quantities along the subsolar line for the equatorial plane (d) and against the  $Y$  axis at  $Z=0$  for the two  $X$  cuts (e and f). The bottom row shows the gradient of the logarithmic values of the four quantities along the subsolar line for the equatorial plane (g) and against the  $Y$  axis at  $Z=0$  for the two  $X$  cuts (h and i). The dash vertical lines in g-i mark the unity locations for two quantities with the innermost and outmost positions, color coded the same as the solid lines.

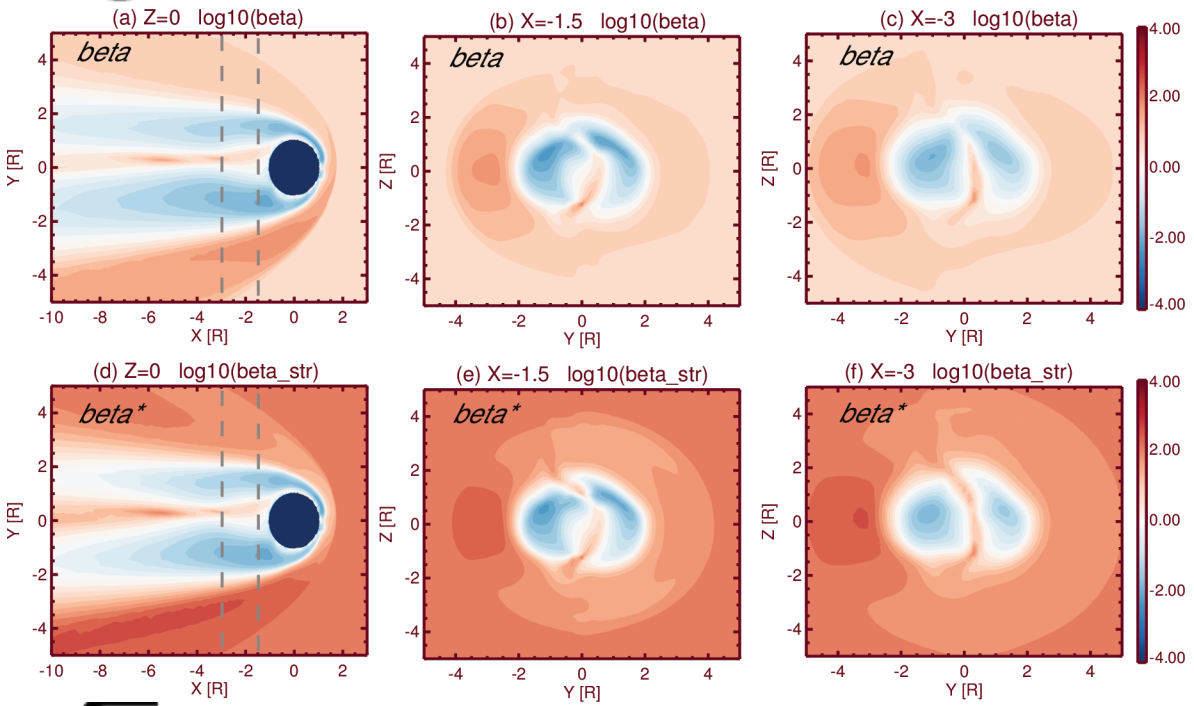
# Author Manuscript

Figure 10 Heavy ion mass density (black),  $H^+$  density (blue), and the ratio of  $H^+$  density and heavy ions (red) against X axis. The unit for mass density is  $\text{amu cm}^{-3}$ , where amu is the atomic mass unit.



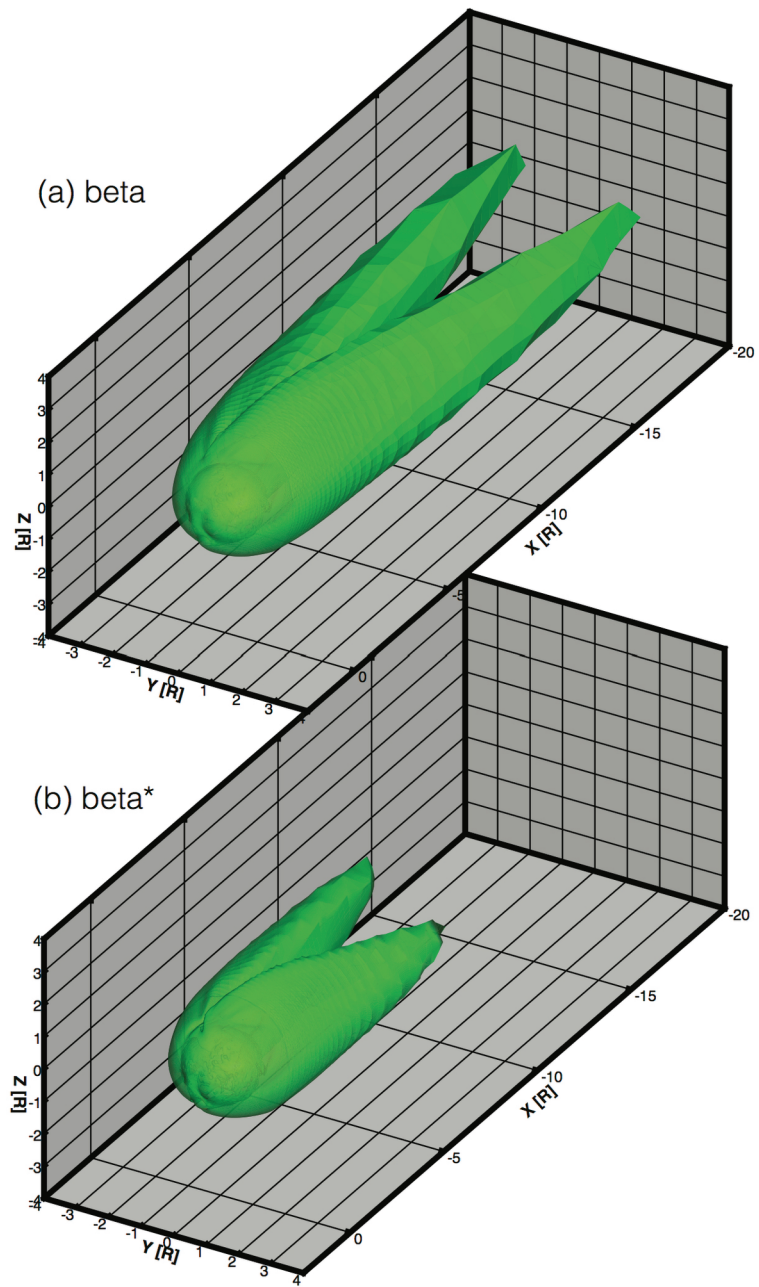
2016ja022644-f01-z-.eps

cript



Auth

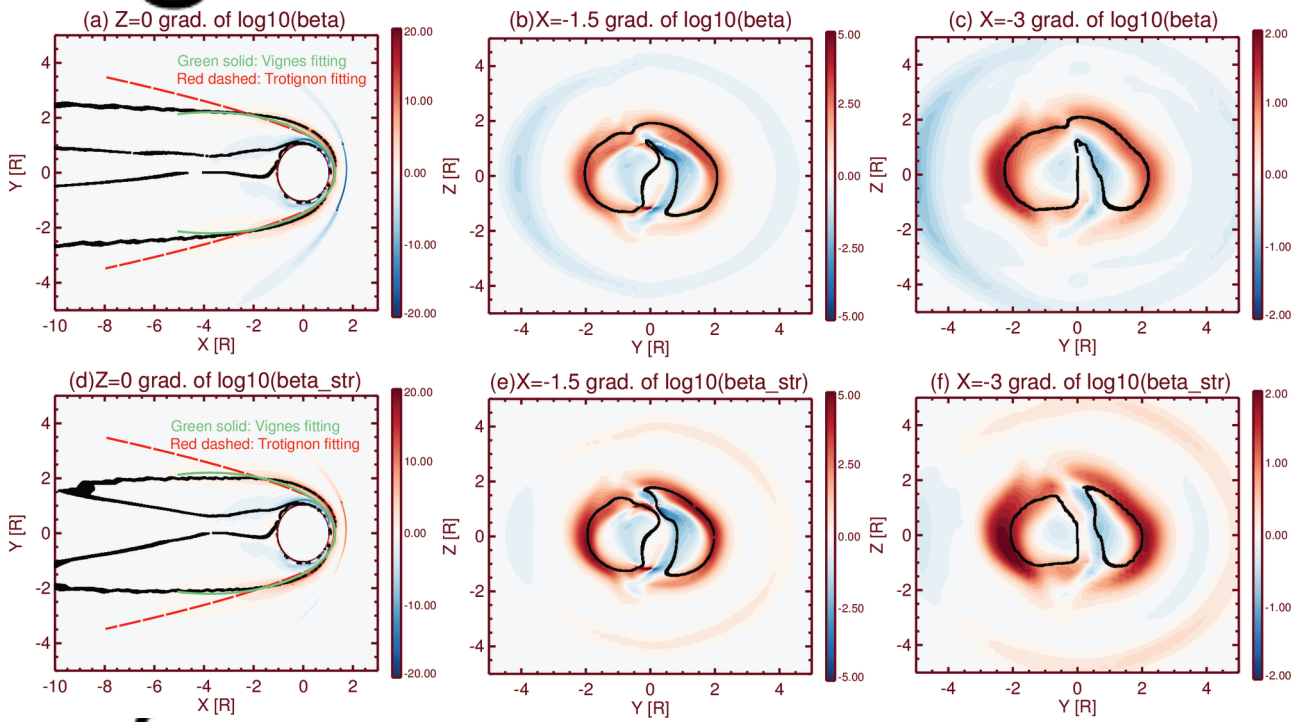
2016ja022644-f02-z-.eps



2016ja022644-f03-z-.eps



cript

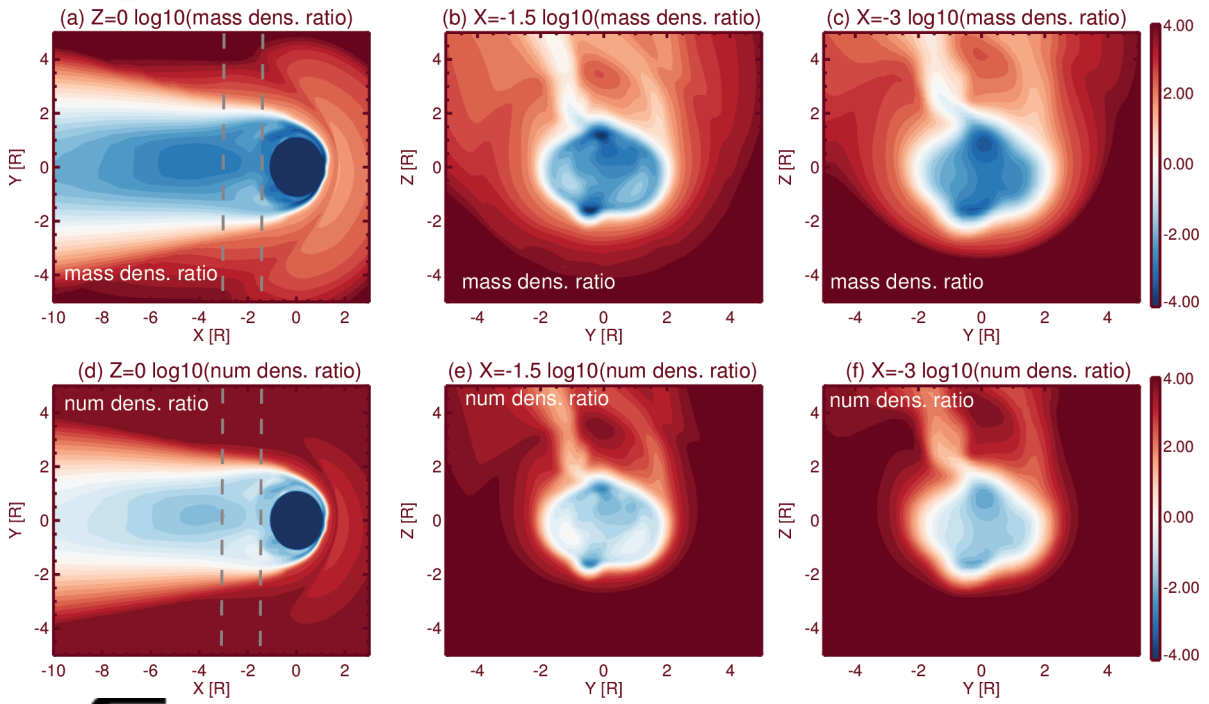


Autr

2016ja022644-f04-z-eps

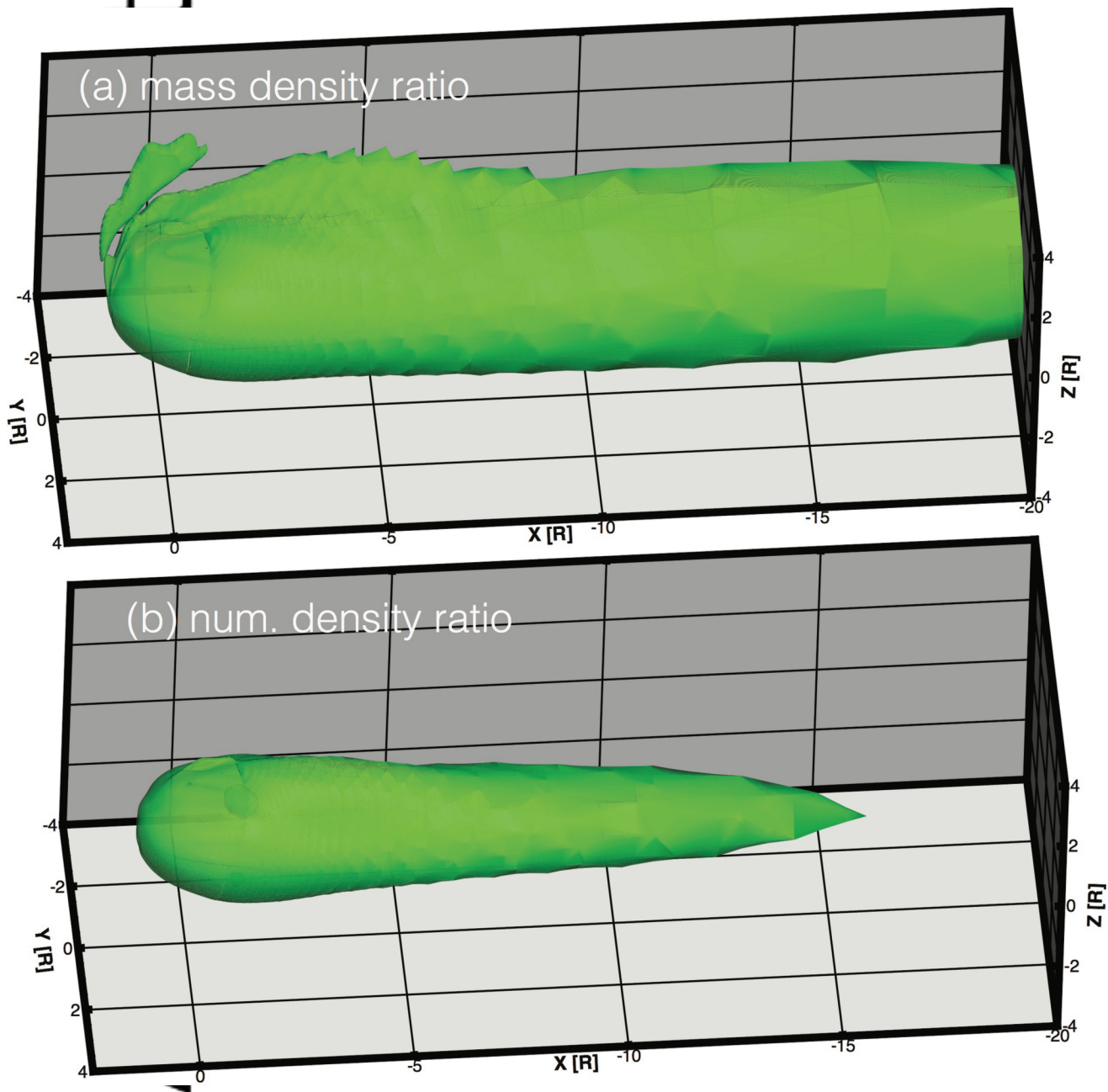


cript



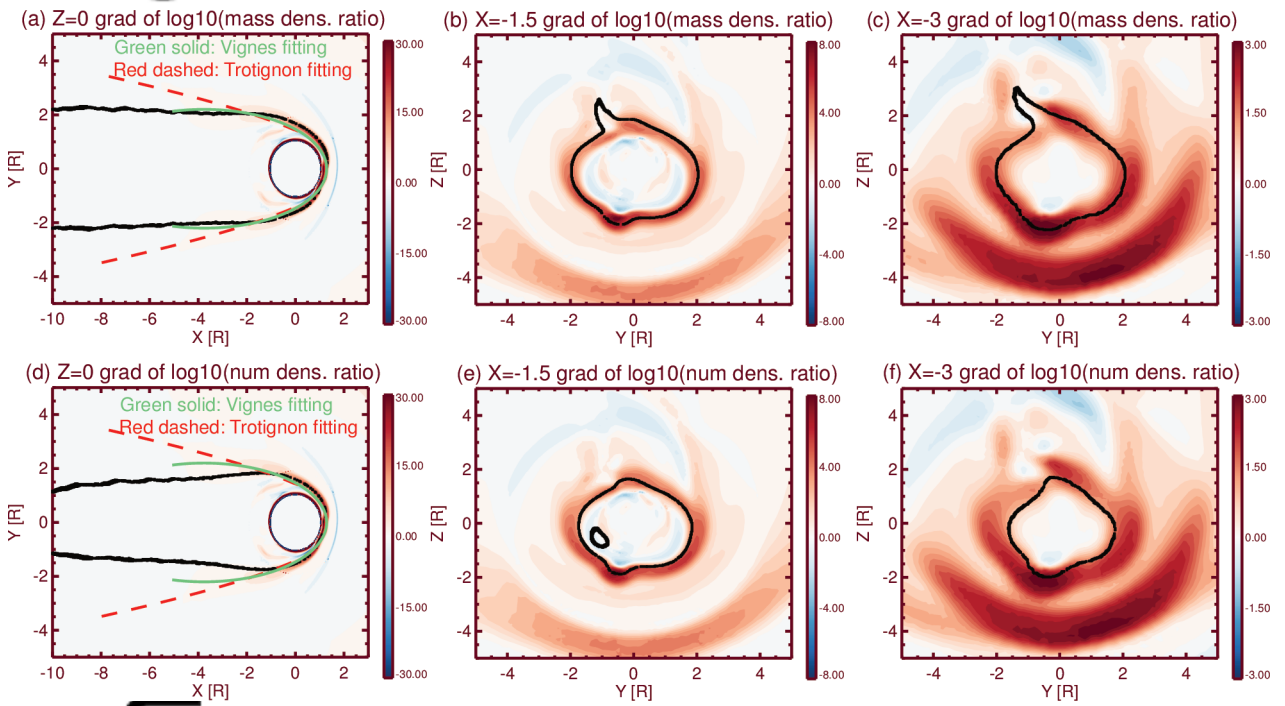
Auth

2016ja022644-f06-z-.eps



2016ja022644-f07-z-.eps

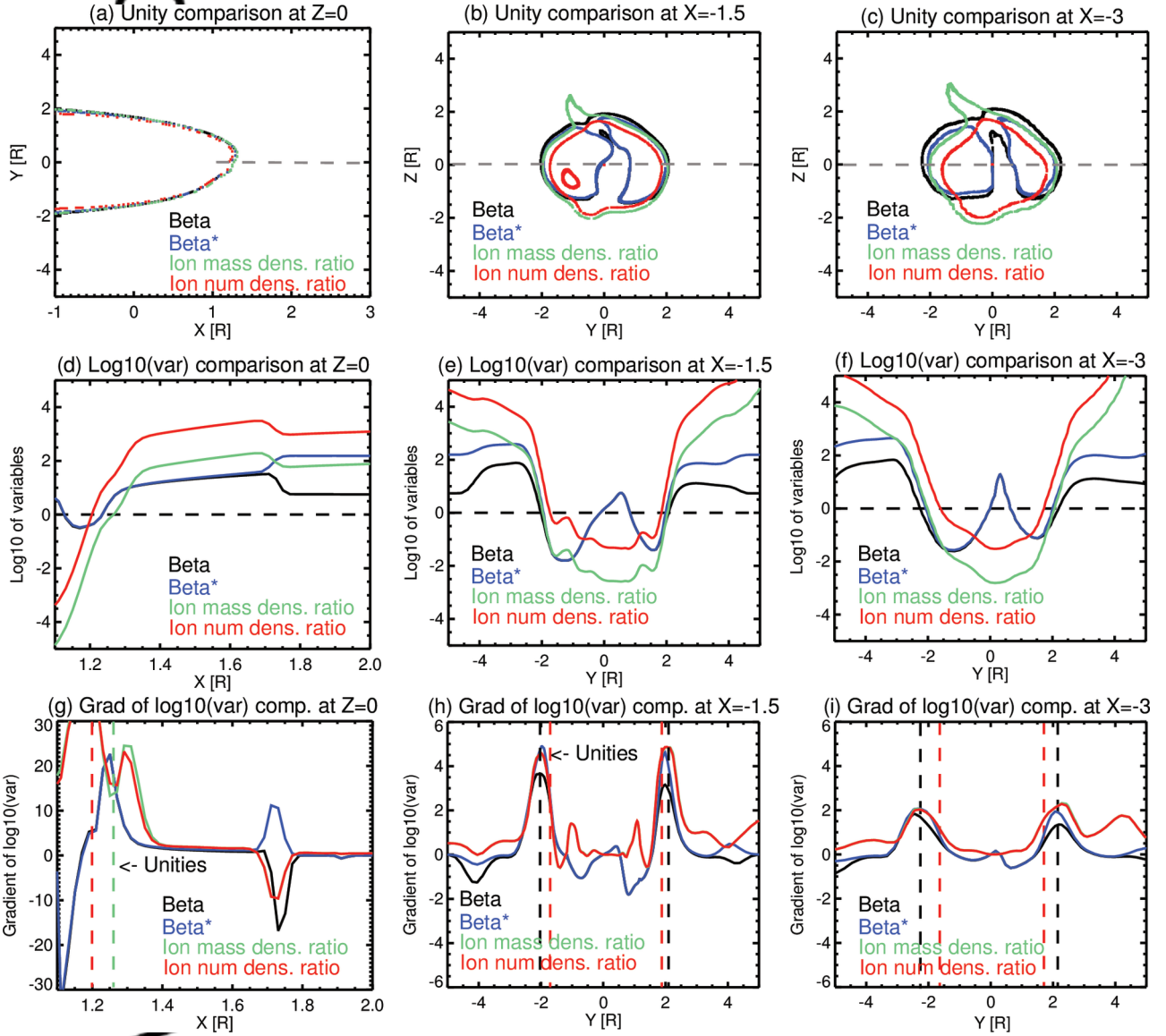
cript



Auth

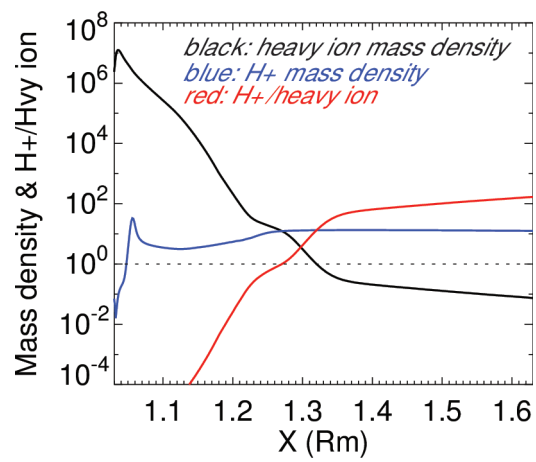
2016ja022644-f08-z-.eps

dt



A

2016ja022644-f09-z-.eps



2016ja022644-f10-z-.eps